Structure-Properties Relationship in Iron Oxide-Reduced Graphene Oxide Nanostructures for Li-Ion Batteries

Seung-Ho Yu, Donato E. Conte, Seunghwan Baek, Dong-Chan Lee, Seung-Keun Park, Kyung Jae Lee, Yuanzhe Piao, Yung-Eun Sung, and Nicola Pinna**

Non-aqueous sol-gel routes involving the reaction of metal oxide precursors in organic solvents (e.g., benzyl alcohol) at moderate temperature and pressure, offer advantages such as high purity, high reproducibility and the ability to control the crystal growth without the need of using additional ligands. In this paper, a study carried out on a series of iron oxide/reduced graphene oxide composites is presented to elucidate a structure-properties relationship leading to an improved electrochemical performance of such composites. Moreover, it is demonstrated that the easy production of the composites in a variety of temperature and composition ranges, allows a fine control over the final particles size, density and distribution. The materials obtained are remarkable in terms of the particle's size homogeneity and dispersion onto the reduced graphene oxide surface. Moreover, the synthesis method used to obtain the graphene oxide clearly affects the performances of the final composites through the control of the restacking of the reduced graphene oxide sheets. It is shown that a homogeneous and less defective reduced graphene oxide enables good electrochemical performances even at high current densities (over 500 mAh/g delivered at current densities as high as 1600 mA/g). The electrochemical properties of improved samples reach the best compromise between specific capacity, rate capability and cycle stability reported so far.

1. Introduction

The need for higher energy and power densities has been explosively growing in recent days. As main power sources of electrical devices such as laptop computers and cellular phones and electrical vehicles, lithium ion batteries (LIBs) have shown their excellence in terms of long cycle life, low maintenance, high power density and high energy density.[1–3] Graphite, which is used as anode in commercial LIBs, is not able to meet the customers' requirements with its limited specific capacity and rate capability. Therefore, it is urgent to develop new materials to replace graphite anodes. However, improvement of both the specific capacity and rate capability at the same time is very difficult. To achieve this, metal and metal oxide nanoparticles-reduced graphene oxide composites have been recently introduced by many research groups.[4–10]

In these composites, the nanometer-sized metal or metal oxide particles such as Si, Sn, SnO_2 and Fe_3O_4 can react with a large amount of lithium. Reduced graphene oxide helps to faster the electron transport between nano-sized particles and the current collector. Moreover, it supports the nano-sized particles, preventing their aggregation during repeated cycling. In addition, reduced graphene oxide itself can store lithium.[11,12] Also, other reduced graphene oxide properties such as intrinsic defects and the number of stacked layers were found to have an influence on the electrochemical properties of reduced graphene oxide-based electrodes.[13,14]

In these electrodes, setting aside the properties of the reduced graphene oxide, the characteristics of the nanoparticles have also been found to strongly affect the electrochemical properties. For example, the sizes of nanoparticles such as Si and SnO_2 were found to be critical for a good electrochemical behavior.[15,16]

S.-H. Yu, S. Baek, D.-C. Lee, K. J. Lee, Prof. Y.-E. Sung, Prof. N. Pinna
School of Chemical and Biological Engineering
College of Engineering
Seoul National University (SNU)
Seoul, 151-744, Korea
E-mail: ysung@snu.ac.kr
S.-H. Yu, K. J. Lee, Prof. Y.-E. Sung
Center for Nanoparticle Research
Institute for Basic Science (IBS), Seoul 151-742, Korea

Dr. D. E. Conte, Prof. N. Pinna
Department of Chemistry
CICECO, University of Aveiro
3810-193, Aveiro, Portugal
S.-K. Park, Prof. Y. Piao
Department of Nano Science and Technology
Seoul National University
Suwon, 443-270, Korea
Prof. N. Pinna
Humboldt-Universität zu Berlin
Institut für Chemie
Brook-Taylor-Straße 2, 12489 Berlin, Germany
E-mail: nicola.pinna@hu-berlin.de

DOI: 10.1002/adfm.201300190

Our group recently developed a general microwave assisted non-aqueous sol-gel approach for the synthesis of metal oxide/reduced graphene oxide nanostructures.[17] The synthesis of the metal oxide nanoparticles involved the microwave assisted solvothermal reaction of tin(IV) chloride or iron(III) acetylacetonate in benzyl alcohol.[18,19] Such an approach is nowadays discussed as the "benzyl alcohol route".[20–23] In this particular case, benzyl alcohol acts as a reactant for the synthesis of the metal oxides and as a reducing agent leading to the partial reduction of graphene oxide.[17] Moreover, it was also proven that the "benzyl alcohol route" greatly benefits from microwave heating by decreasing the reaction time to just minutes for nanoparticle formation.[24,25]

Compared to the numerous approaches that were recently reported for the synthesis of such composites our approach has the advantage of being carried out in only one step, very rapidly (5–10 min), leading to gram quantities of nanocomposites, and to in situ selectively grown metal oxide nanoparticles at the surface of graphene oxide, which is simultaneously reduced during the synthesis.

The main purpose of this work is to investigate and discuss how structural aspects (*e.g.* particle size and density, restacking of reduced graphene oxide, preparation method of the graphene oxide, etc.) affect the electrochemical properties of the composites in terms of specific capacity, rate capability and life time. The focus of this study is on the iron oxide-reduced graphene oxide system. We will show that by optimizing the structural properties of both the oxide and reduced graphene oxide phases we could determine the factors influencing the performances of the anodes and reach the best compromise between specific capacity, rate capability and cycle stability reported so far.

2. Results and Discussion

2.1. Synthesis

Scheme 1 illustrates the preparation process of iron oxide/reduced graphene oxide composites. After all the reactants (Fe(III) acetylacetonate, GO, benzyl alcohol) had been mixed together, sonication for 2 h was applied to disperse the aggregated GO. $Fe(acac)_3$ reacts with the oxygenated groups present at the surface of the GO that act as nucleation sites for the iron oxide nanoparticles, which are formed under microwave irradiation in short time. Simultaneously GO is partially reduced by benzyl alcohol. In this reaction, benzyl alcohol plays the dual role of reactant for the formation of the metal oxide nanoparticles and of reducing agent, resulting in the partial reduction of GO.[17] The microwave irradiation offers a more homogeneous heating compared to traditional heating methods. Moreover, as previously demonstrated, benzyl alcohol is a bad microwave absorber compared to GO making this approach appealing for the preferential heating of the GO, leading to its homogeneous coating with nanoparticles (see below and ref. [17]). Using this approach, it was possible to synthesize up to 2 g of powder in 20 mL of benzyl alcohol after only 10 min of microwave irradiation (Figure S1, Supporting Information). For the sake of comparison (cf. below), the same procedure was employed to treat GO but without the addition of metallic precursors. In this study, two types of GO were prepared. One type has been obtained by the Hummers' method (GO1), while the other was prepared by a modified Hummers' procedure (GO2).

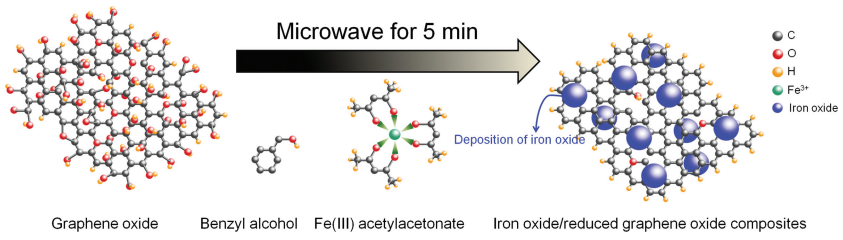

Scheme 1. Procedure of iron oxide/reduced graphene oxide composites fabrication.

2.2. Structural and Chemical Properties

Table 1 summarizes the experimental conditions, the crystallite sizes (from Rietveld refinements), the estimated reduced graphene oxide weight ratio, the ratio between the TG weight loss between 300 and 600 °C and that between 200 and 600 °C, the BET specific surface area and the I_D/I_G ratio (from Raman spectra) for the indicated iron oxide/reduced graphene oxide composites. The reduced graphene oxide weight ratio was estimated from TGA experiments (*cf.* Figure S3 in the Supporting Information). Two values are presented, the first value is considered to be the amount of fully reduced graphene oxide (corresponding to the weight loss from 300 to 600 °C) while the second value, shown inside brackets, is considered to be the total amount of reduced graphene oxide, including the oxygen-containing functional groups (weight loss from 200 to 600 °C). In fact, a similar approach[26] showed that a high weight fraction attributed to the removal of oxygenated functional groups can be observed around 250 °C from TGA experiments.

It can be noticed that the values obtained for the ratio of TG weight loss (300–600 °C over 200–600 °C), the surface area and the I_D/I_G ratio allow dividing the samples into two groups: IG1 to IG6 and IG7-IG8. It is clearly visible that the reduced graphene oxide obtained by the two different methods (GO1 and GO2) have different characteristics. The I_D/I_G values of the composites prepared with GO1 (IG7 and IG8) are higher than those of the composites obtained with GO2 (over 1.4 for the former and in the range 1.2 to 1.3 for the latter). This indicates that GO1 is more likely to have dangling bonds, vacancies, and topological defects[13] with respect to GO2. In addition, the BET surface areas of IG1-IG6 are consistently higher (over 160 m^2/g) than those of IG7 and IG8, indicating a better and more homogeneous particle growth on the GO2. Accordingly, the values of the TG weight loss ratio of IG1-IG6 are much lower than those of IG7 and IG8, meaning that the reduced graphene oxide of the IG1-IG6 series has more functional groups.

In order to acquire information on the crystallinity and structural properties of the samples, powder XRD experiments and Rietveld refinements were carried out for each sample (**Figure 1** and S2 in the Supporting

Table 1. Experimental conditions, crystallite sizes (from Rietveld refinements), reduced graphene oxide weight% estimated by TGA, TG weight loss between 300 to 600 °C divided by TG weight loss between 200 to 600 °C, BET specific surface area and I_D/I_G ratio (from Raman spectra) of the iron oxide/reduced graphene oxide composites. The amount of benzyl alcohol used in the synthesis was kept constant (20 mL) for all samples.

Sample name	Metal oxide precursor [mmol]	GO type	GO [g]	Reaction T [°C]	Reaction time [min]	Yield [g]	Crystallite Size [nm]	Graphene weight%	$C_{(300\text{-}600)}/C_{(200\text{-}600)}$%	BET surface area [m^2/g]	I_D/I_G
IO	15		0	180	10	0.89	5.4(7)	-		98	-
IG1	3	GO2	0.10	200	5	0.33	5.4(4)	19.3(24.8)	77.8	213	1.236
IG2	3	GO2	0.20	200	5	0.37	6.5(8)	23.6(27.2)	86.8	177	1.254
IG3	3	GO2	0.30	200	5	0.46	6.3(3)	41.1(47.4)	86.7	167	1.280
IG4	3	GO2	0.30	220	5	0.51	5.6(5)	27.3(31.0)	88.1	170	1.186
IG5	3	GO2	0.30	180	5	0.52	3.4(6)	35.3(45.6)	77.4	178	1.244
IG6	3	GO2	0.30	160	5	0.40	-	36.1(50.5)	71.5	181	1.276
IG7	3	GO1	0.30	200	5	0.48	4.3(7)	45.5(49.3)	92.3	148	1.529
IG8	3	GO1	0.40	200	5	0.57	4(1)	50.4(53.6)	94.0	125	1.411

Information, and **Table 2**). The IG6 sample exhibits low intensity and extremely broad diffraction peaks due to low crystallinity (cf. also TEM analysis), so Rietveld refinement was not possible for this sample. The Rietveld refinement of the IG4 pattern recorded at room temperature is reported in Figure 1a. The refinement can be conducted using the regular cubic unit-cell for magnetite (space group $Fd\bar{3}m$) resulting in a cell parameter slightly lower than that reported in the JCPDS file #04-014-0193 (839.42 pm): a = 836.4(1) pm. The broadening of the diffraction peaks is typical of the presence of nanometric crystallites which results in an average size of 5.6 nm. It is worth noting that, the general trend for magnetite cell parameters, is to reach a value halfway between that of the pure magnetite (839.42 pm) and that reported for the similar maghemite, γ-Fe_2O_3 (space group $Fd\bar{3}m$, a = 833.00 pm[27]). When attempting to treat the recorded pattern with both these phases, a convergence of both of them towards the average value of 836 pm has been noticed. It is well known that γ-Fe_2O_3 (maghemite) can be considered as a magnetite with a fraction of the octahedral Fe^{2+} sites free.[28] Now, it is accepted that the maghemite crystallizes in the cubic system but Pernet et al.[29] observed extra diffraction lines in the region $10 < 2\theta < 30°$. The same lines have been more recently observed during the development of a benzylamine-based synthesis of iron oxides[30] (peaks at 23.8 and 26.1 $2\theta°$). Ho, et al.[31] clarified that maghemite could only crystallize in a cubic system and that the extra diffraction lines are due to ordering of the octahedral Fe^{2+} vacancies. In Figure 1b inset, two very small and broad peaks appear at 23.8 and 26.4 $2\theta°$ for the pure sample (asterisks on the black line) suggesting the formation of maghemite instead of magnetite. Actually, the reported cell parameters with a value halfway between those of magnetite and maghemite, let us hypothesize the simultaneous presence of the two phases. Thus, from XRD analysis it is not possible to exclude the presence of maghemite. Further discussion of the phase determination will be given below on the basis of x-ray absorption experiments.

The increase in the quantity of reduced graphene oxide in the composites results in a sloping effect on the recorded XRD patterns. A similar effect has been reported during charcoal carbonization tests for samples reacted at 350 °C.[32] The authors attributed this behavior to the presence of turbostratic crystallites inside an amorphous carbon phase at low carbonization temperatures.[32]

The general observation done above is valid for both series of composites obtained with graphene oxide prepared by different synthesis procedures (*cf.* the Experimental Section). The contribution due to the restacking of reduced graphene oxide is present in the XRD patterns of iron oxide/reduced graphene oxide composites and it is centered at around 25 $2\theta°$ and tends to increase in intensity with the increase of the graphene oxide content (Figure 1b). It should be noted that the composites synthesized from GO prepared from the standard Hummers method (IG7 and IG8) present a much

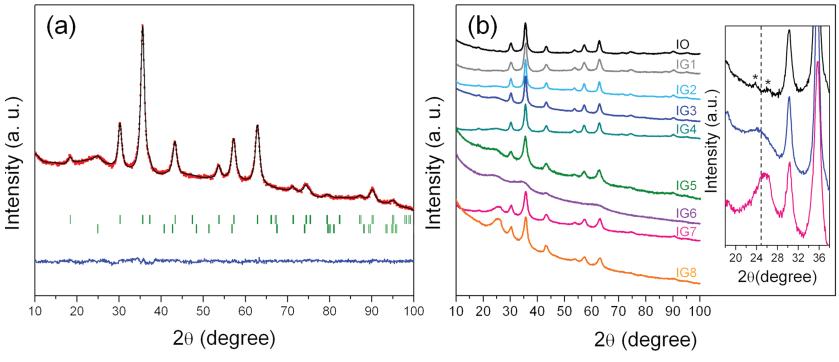

Figure 1. a) Rietveld refinement of the IG4 composite XRD pattern (λ = 154.18 pm, 300 K). Bragg positions (green) for magnetite (above) and graphite (below) are indicated. Observed data (red squares), fitting curve (black line) and difference curve (blue line) are also reported. b) XRD patterns ofiron oxide/reduced graphene oxide composites recorded at 300 K. The enlargement of the region $18 < 2\theta < 38°$ of IO, IG3 and IG7 (inset), highlights the evolution of the reduced graphene oxide peak at around 25 $2\theta°$. Asterisks mark the extra lines due to ordering of the octahedral Fe^{2+} vacancies (see the Results and Discussion section).

Table 2. Lattice constants and Rietveld refinement results from X-ray diffraction ($\lambda = 154.18$ pm) for various iron oxide/reduced graphene oxide composites at 300 K.

Sample name	a [pm]	Fe1; Fe2 atomic positions [x, y, z]	O atomic positions [x, y, z]	B_{iso} [Fe1, Fe2]	B_{iso} [O]	R_{Bragg} [%]	Total χ^2
JCPDS 04-014-1396	839.42		0.2544, 0.2544, 0.2544	0.8, 0.7	1.0	/	/
IO	835.0(1)		0.256(1), 0.256(1), 0.256(1)	2.4(1), 2.1(1)	1.6(1)	2.31	1.92
IG1	835.6(1)		0.250(1), 0.250(1), 0.250(1)	1.8(1), 2.4(1)	1.3(1)	2.94	1.91
IG2	836.2(1)		0.249(1), 0.249(1), 0.249(1)	2.5(1), 2.5(1)	1.0	1.58	2.41
IG3	836.0(1)	0.125, 0.125, 0.125;	0.255(1), 0.255(1), 0.255(1)	4.1(2), 3.2(1),	1.0	2.10	2.47
IG4	836.4(1)	0.5, 0.5, 0.5	0.253 (1), 0.253(1), 0.253(1)	1.9(1), 2.7(1)	1.3(1)	2.00	1.90
IG5	837.3(1)		0.252(1), 0.252(1), 0.252(1)	3.6(1), 3.6(1)	1.0	3.36	1.56
IG6	-		-	-	-	-	-
IG7	834.7(1)		0.250(1), 0.250(1), 0.250(1)	2.2(2), 3.3(2)	1.7(2)	1.26	1.91
IG8	834.9(1)		0.245(1), 0.245(1), 0.245(1)	2.9(2), 2.9(2)	1.6(3)	1.43	2.66

more pronounced peak at around 26 2θ°. The reflections from the (002) family of planes is reported to appear at 26.38 2θ° in the reference JCPDS file of graphite #04-014-0362 while the same reflection appears at 25.97 2θ° for IG7 and at 25.92 2θ° for IG8. This observation points out to a better exfoliation and a lower tendency to restack in the nanocomposite samples prepared from GO derived from the modified Hummers method (GO2) as compared to the original approach (GO1).

As demonstrated by Rietveld analysis it was possible to tune the iron oxide crystallite sizes, ranging from approximately 3.5 to 6.5 nm, by increasing the reaction temperature (*cf.* Table 1). Furthermore, the GO source has also an influence on the crystallite size, which is sensitively smaller on the GO produced via the original Hummers method.

X-ray absorption near edge spectroscopy (XANES) was performed to discriminate magnetite and maghemite using the difference of oxidation state of Fe (average oxidation states of magnetite and maghemite are +2.67 and +3, respectively) (**Figure 2**a). The commercial nano-sized (<50 nm) Fe_2O_3 (No. 544884 from Aldrich, primarily maghemite) and Fe_3O_4 (No. 637106 from Aldrich) powders were used as references. The peak of IG6 is ill defined and broadened due to its low crystallinity.[33,34] The 1s→3d pre-edge is normally forbidden, but it is observed experimentally due to the electric quadrupole coupling.[34–36] The pre-edge position is a sensitive indicator of the relative fraction of Fe^{2+} and Fe^{3+},[33,34,37] and it is shown in the inset of Figure 2a. The gap of pre-edge positions of commercial Fe_2O_3 and Fe_3O_4 is smaller than that reported in the literature while the pre-edge position of commercial Fe_3O_4 is higher. This effect could be attributed to partial oxidation on the surface of the nano-sized commercial Fe_3O_4.[33,34] The positions of pre-edge peaks are obtained from derivatives of the Fe K-edge profiles. The oxidation states of Fe for the iron oxide/reduced graphene oxide composites fall in the middle region between those of commercial maghemite and magnetite. This is in agreement with the XRD treatment of the cell parameters as explained above. As visible in Figure 2b, there seems to be a trend related to the final reduced graphene oxide content in the sample. The higher the GO content is, the lower the Fe average oxidation state and higher the cell parameter (i.e., the magnetite phase is favored). This behavior is probably related to the reducing effect of the *in situ* reduced GO.

In order to analyse the surface elemental composition and chemical states for the iron oxide/reduced graphene oxide composites, we performed X-ray photoelectron spectroscopy (XPS, **Figure 3**).

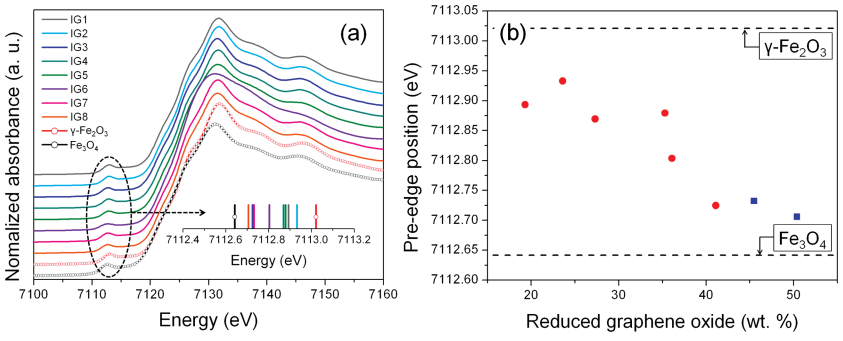

Figure 2. a) XANES spectra at Fe K-edge for iron oxide/reduced graphene oxide composites. The reference samples are nano-sized powders (<50 nm) of γ-Fe_2O_3 and Fe_3O_4. The inset shows the positions of pre-edge peaks. b) Relationship between pre-edge positions and reduced graphene oxide contents. Red circles are related to GO2 while blue squares are related to GO1 composites.

The survey spectra (Figure 3a) reveal that no other element is present on the surface other than C, O and Fe. The C 1s peaks of the composites (Figure 3b), show that C-C (284.6 eV) signals are clearly predominant with small contributions of C-O (286.5 eV), C = O (288.1 eV) and O-C = O (289 eV) suggesting that the graphene oxide is well reduced as we confirmed in a previous study.[17] No significant difference is found between the surface carbon contribution in the samples prepared from the two sources of graphene oxide: GO1 (IG7 and IG8) and GO2 (IG1-IG6). In the Fe 2p region of the spectra (Figure 3c), the Fe $2p_{3/2}$ peaks are located between those of commercial

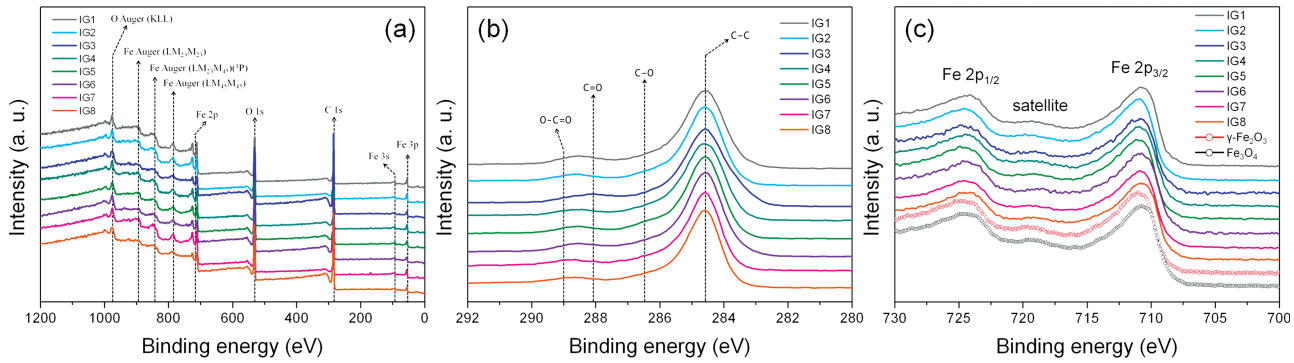

Figure 3. XPS spectra of the iron oxide/reduced graphene oxide composites: a) survey scans; high resolution scans of b) C 1s and c) Fe 2p region.

Fe_2O_3 and Fe_3O_4. The satellite peaks (region between Fe $2p_{3/2}$ and Fe $2p_{1/2}$) are characteristic of Fe^{3+} in Fe_2O_3 and are present in all samples including commercial Fe_2O_3 and Fe_3O_4.[38] Additionally, the Fe $2p_{3/2}$ peak position for the commercial Fe_2O_3 is 711.0 eV, in good agreement with previous reports, but the Fe $2p_{3/2}$ peak position of the commercial Fe_3O_4 is slightly higher than that of Fe_3O_4 reported in the literature.[38] These results agree well with the XANES and XRD results and clearly point out that most probably mixed oxides are produced by the microwave assisted "benzyl-alcohol route".

The correlations between the GO weighed for the synthesis, the final reduced graphene oxide contents and the BET surface area are shown in **Figure 4**. As already pointed out, the final reduced graphene oxide content increases with the increase of the initial weighed GO. More interestingly, the BET surface area linearly decreases with the increase of the amount of GO. This can be explained by the restacking of reduced graphene oxide layers that is effectively prevented when the iron oxide amount is higher.

TEM images of the composites show that the reduced graphene oxide is covered by a homogeneous layer of iron oxide nanoparticles, which, depending on the synthesis conditions, can even reach continuous fully packed nanoparticles films (**Figure 5**). For reactions performed at the same temperature, but with increasing GO content (IG1 to IG3), the particle density onto the reduced graphene oxide decreases (Figure 5a–c,e,f). As a matter of fact for the sample (IG3) the iron oxide particles appear to be more spaced from each other. This was expected considering the reduced relative amount of iron precursors compared to GO. In Figure 5e–i, the different particle sizes can be ascribed to different reaction temperatures applied. There is a decrease in size from 200–220 °C down to 160 °C, in agreement with the crystallite size determination from XRD and Rietveld analysis. It is interesting to mention that IG7, obtained with GO1, has smaller iron oxide particles than IG3, obtained with GO2, although both samples were synthesized at the same temperature (*cf.* XRD analysis). This behavior might be related to the concentration of surface defects, with a higher concentration leading to a higher nucleation density and therefore to smaller particles in the final material. Taking into consideration Table 1, the average I_D/I_G ratio obtained from Raman spectroscopy for IG3 is 1.28. The same ratio appears to be considerably higher for IG7 (1.53). Being I_D (D band) and I_G (G band) the intensities of the Raman bands centered at 1340 and 1600 cm^{-1}, respectively. The G band corresponds to the stretching mode of the C–C bond in the graphitic plane and demonstrates the presence of crystalline graphitic carbon. On the other hand, the D band originates from defects and amorphous carbon. An increase of the I_D/I_G ratio translates into a higher number of defects (sp^3 bonded carbon, dangling bonds, vacancies, etc.) on the graphene surface.[13] For this reason, the nucleation of iron oxide nanoparticles can be better induced on the surface of GO1 compared to the GO2. This of course would lead to a higher number of nuclei per area, which would result in smaller average sizes and eventually to a continuous and conformal film onto the reduced graphene oxide. Similar, nucleation effects are commonly observed on the atomic layer deposition of metal oxides onto carbon based nanostructures.[39]

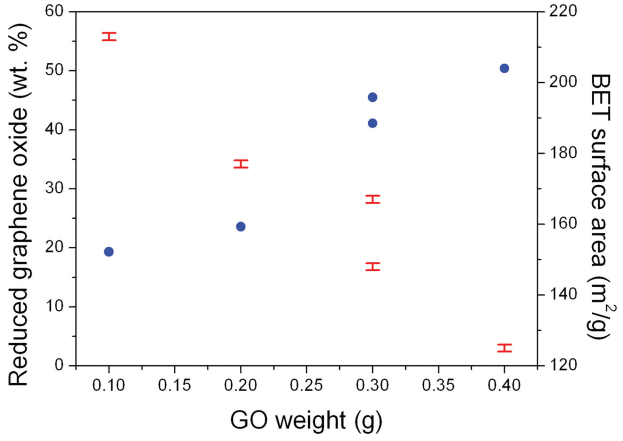

Figure 4. Correlations between GO weight, reduced graphene oxide content in the composite (blue symbols) and BET surface area (red symbols). The reaction temperature (200 °C), the amount of benzyl alcohol and the reaction time were kept constant for all samples.

In order to further assess the homogeneity of the particles over the reduced graphene oxide surfaces, particle size distribution functions were calculated from the recorded XRD patterns (**Figure 6**). It should be noted that such functions do not directly represent the particle size distributions, but instead give their trend. Moreover, it is also important to stress that the average crystallite size values reported in Table 1 (spots in

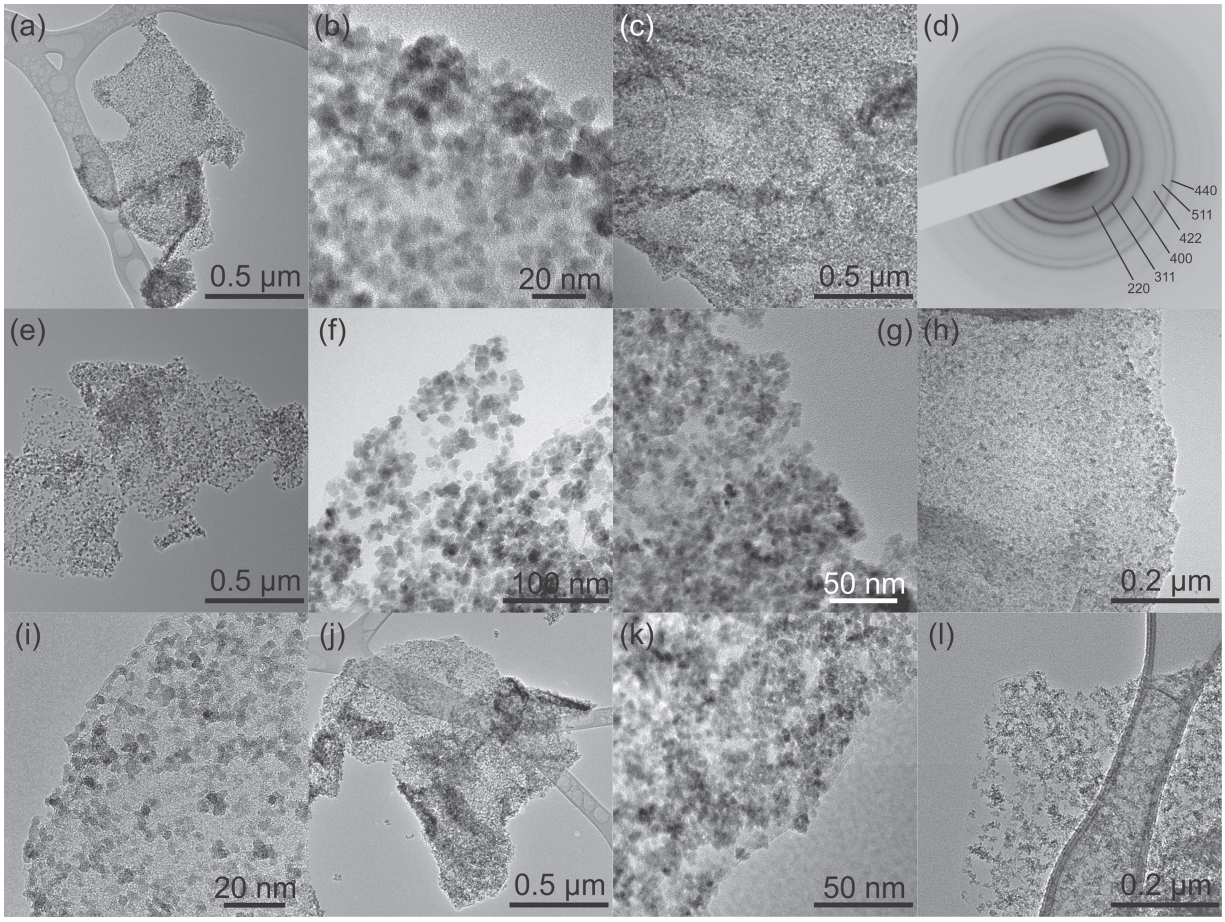

Figure 5. Transmission electron microscopy images of iron oxide/reduced graphene oxide composites. a,b) Overview and magnification of an edge region of IG1. c) Magnification of an edge region of IG2. d) SAED pattern of IG2. e,f) Overview and magnification of an edge region of IG3. g–i) Magnification of an edge region of IG4, IG5 and IG6, respectively. j,k) Overview and magnification of an edge region of IG7. l) Magnification of an edge region of IG8.

Figure 6), do not represent the peak of the functions in Figure 6 but rather the median value as expressed in Equation 4 (see the Experimental Section for additional details).

The samples IG1 to IG3 have been synthesized at the same temperature but with increasing GO content. For these samples, the density of particles on the reduced graphene oxide decreased resulting from the reduced relative amount of iron precursors compared to GO. The particle size distribution functions for these samples (Figure 6a) provide some additional information: the distribution function of IG1 is clearly more symmetric and narrower with respect to those for IG2 and IG3. Larger and asymmetric functions suggest the presence of a small amount of larger particles, here in the region above 10 nm, clearly in agreement with the TEM observations: the presence of some larger particles along with the decrease of the relative amount of iron compared to GO can easily result in a more spaced distribution of particles over the accessible GO surface. Thus, for the same reaction temperature and initial iron precursor content, smaller amounts of GO2 allow a more homogeneous particle growth as well as a better distribution over the carbonaceous surface.

When we compare samples prepared at different reaction temperatures, keeping the other parameters constant (IG3 to IG5 samples in Figure 6a), there is a clear difference when the initial suspension is heated below 200 °C. On the other hand, there is not much variation between the IG3 (200 °C) and IG4 (220 °C) distribution functions: both have a very similar peak position and tail shape. For IG5 (180 °C), the distribution function becomes particularly narrow and shifted to small particle sizes.

When we compare materials synthesized with different carbonaceous substrates, we find that IG7, obtained with GO1, has smaller iron oxide particles compared to IG3, obtained with GO2. This behavior might be related to the concentration of surface defects (e.g., oxygenated species), as a higher defect concentration will lead to a higher nucleation density and therefore to smaller particles in the final material. The effect is very similar to what has been observed for the IG1 to IG3 series (Figure 6b). The distribution function of IG7 is clearly more symmetric and narrower with respect to that of IG3.

Similar trends concerning the iron oxide particle sizes are observed in the high resolution TEM (HRTEM) images

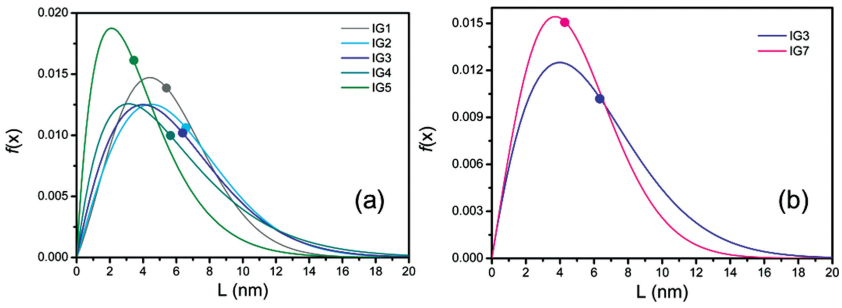

Figure 6. Particle size distribution functions ($f(x)$) of IG series obtained with a) GO1 and b) comparison between IG3 and IG7. Functions were calculated by XRD data analysis. Average crystallite sizes (from Table 1) are reported as spots on the corresponding curves.

(**Figure 7**a–c). Indeed, the iron oxide particles of sample IG2 are larger than those of IG6 and IG7 with average sizes that correspond well to the crystallite sizes obtained from XRD measurements. For the sample IG6, although no clear diffraction peaks were observed in XRD measurements (see above), small particles with low crystallinity in the order of 2–3 nm are observed in the HRTEM image (Figure 7b). For such a low temperature synthesis, in order to better appreciate the quality of the HRTEM image, a high quality (i.e., not downscaled) image is also added to the Supporting Information (Figure S5). The HRTEM image of an edge region in sample IG7 shows part of stacked reduced graphene oxide layers and iron oxide nanoparticles (Figure 7c). The power spectrum of Figure 7c (i.e., square of the Fourier transform reported in Figure 7d) shows the characteristic reflections of iron oxide. Since both magnetite and maghemite give rise to very similar patterns, at these sizes it is impossible to clearly distinguish both phases, similarly to what was concluded from the XRD studies.

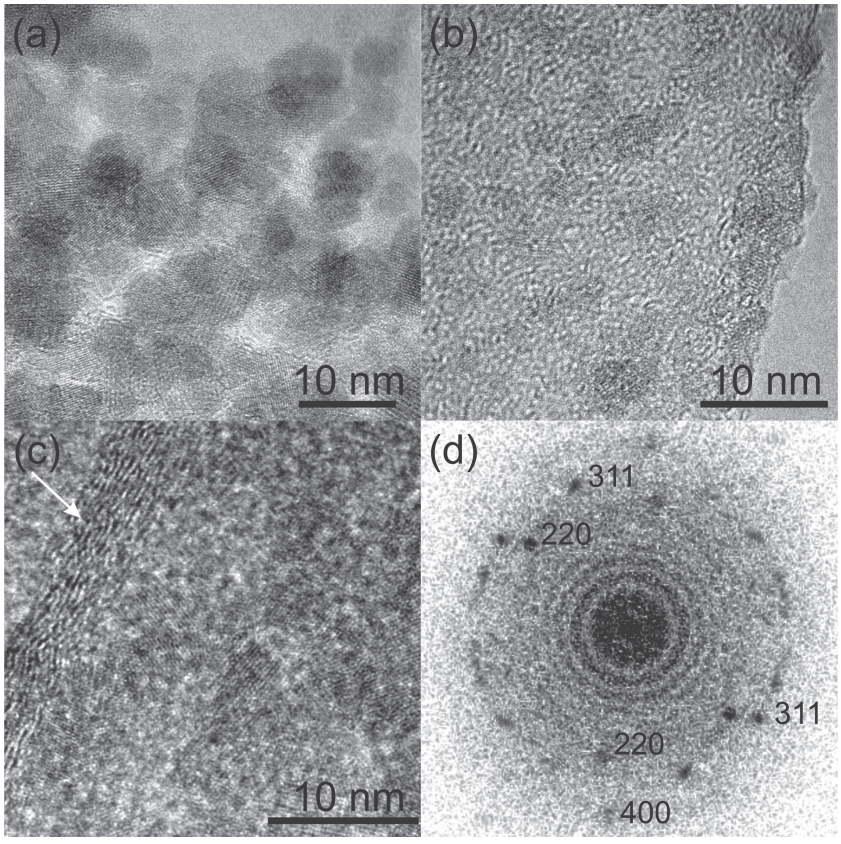

Figure 7. High-resolution TEM Images of a) IG2, b) IG6 and c) IG7. The HRTEM in (c) shows lattice fringes due to the iron oxide nanocrystals as well as the fringes due to several layers of stacked reduced graphene oxide (white arrow). d) Power spectrum of the center of the image in (c).

2.3. Electrochemical Study

In the following part of the article, the electrochemical properties of all the samples described in this study are evaluated, compared and discussed in view of the chemical and structural properties presented above. **Figure 8**a shows charge-discharge voltage profiles of a battery assembly fabricated from IG3. In the first discharge curve (red curve), the long plateau observed around 0.8 V (vs Li^+/Li) is in good agreement with those of magnetite- and maghemite-based anodes previously reported.[40–45] The irreversible capacity in the first cycle is attributed to the electrolyte decomposition and formation of solid electrolyte interface (SEI) layer. Cyclic voltammetry (CV) was conducted to acquire additional information on the electrochemical reactions (Figure 8b). The small reduction peaks at 1.58 and 1.00 V in the first cycle can be ascribed to a lithium intercalation reaction, for low levels of lithiation, leading to the formation of intermediates such as $Li_xFe_3O_4$ and $Li_xFe_2O_3$ ($0 < x < 2$).[44–48] The strong anodic peak centered at 0.63 V corresponds to the reduction of Fe^{3+} and Fe^{2+} to Fe^0, and the electrolyte decomposition and formation of SEI layer.[43–45] The last cathodic peak under 0.3 V is attributed to the reaction of lithium with carbon of the graphene layers.[8] The two anodic peaks at 1.61 and 1.88 V are attributed to the reversible oxidation of Fe^0 to Fe^{2+} and Fe^{3+}, respectively.[43,45] The subsequent CV curves show good reversibility.

The rate properties of all iron oxide/reduced graphene oxide composites, iron oxide nanoparticles and reduced graphene oxide (reduced GO2) are shown in **Figure 9**. The samples prepared with GO1 (IG7 and IG8) have lower surface area, resulting in the lower irreversible capacity loss in the first cycle. As expected, the capacity of electrodes made with bare iron oxide nanoparticles tends to be less stable with respect to the composite materials showing a marked degradation of their performances already at low current densities.[41] However, our iron oxide nanoparticles are also able to withstand relatively high current densities in agreement

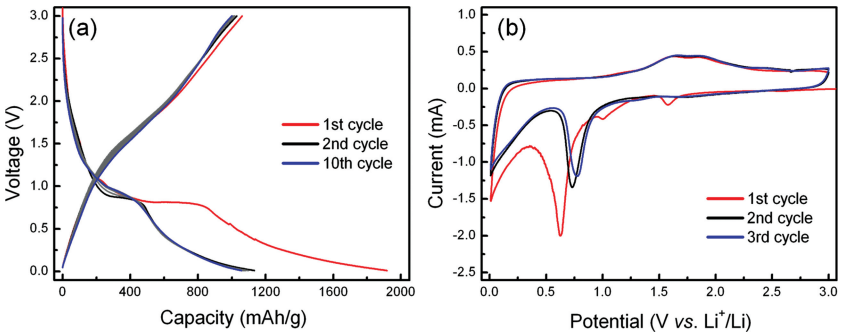

Figure 8. a) Charge-discharge voltage profiles of IG3 during the initial 10 cycles at a current density of 100 mA/g. b) Cyclic voltammograms of IG3 at scanning rate of 0.1 mV/s.

with some previous reports.[49] It is interesting to remark the increase in performance observed between cycles number 50 to 60, as the current density is lowered back to 100 mA/g. This proves that bare iron oxide nanoparticles produced following the "benzyl alcohol route" can be easily processed in electrode fabrications and can also be used as starting battery material for low rate applications.

In order to understand the relationship between chemical and structural characteristics of the samples and the electrochemical properties, the rate performances and voltage profiles are reorganized for three set of samples (**Figure 10**). i) Effect of the source of graphene oxide (Figure 10a–c), ii) effect of the iron oxide/reduced graphene oxide ratio (Figure 10d–f) and iii) effect of the iron oxide particle size (Figure 10g–i). Figure 10a shows the rate properties of IG3 and IG7. Despite the preparation procedure being the same, the two electrodes show large differences in irreversible and reversible capacities. This indicates that the quality of the starting graphene oxide materials strongly affects not only the nanostructure of the final composites, as we discussed above, but also their electrochemical properties. Theoretically, in a condition where all the reduced graphene oxide layers are separated monolayers, each carbon could react with lithium up to a LiC_3 stoichiometry with a maximum capacity of 744 mAh/g.[50] However, in practice the mechanism of graphene is more complex and in many recent reports, graphene delivered over 744 mAh/g.[13,14,51] Moreover, many characteristics such as Raman intensity ratio I_D/I_G,[13] *d*-spacing between graphene sheets[11] and the number of stacked graphene sheets[14] proved to affect the final delivered capacity. In our case, the graphene oxide used for the synthesis of IG3 (i.e., GO2) has been prepared by a modified Hummers' method. Following this approach, two oxidation steps are performed compared to only one for the graphene oxide used in the formation of IG7 (i.e., GO1). IG3 resulted to have higher irreversible and reversible capacities independently of the discharge/charge rate tested. The capacity delivered below 0.8 V can be considered to be mainly due to reaction of lithium ions with graphene. The capacity delivered below 0.8 V of IG3 is much higher than that of IG7 even though the final reduced graphene oxide content is lower in sample IG3 (Figure 10b). We have reason to believe that the higher capacities are linked to the smaller numbers of stacked graphene sheets, characteristic of the samples fabricated from GO2. It should be stressed that these conclusions are in agreement with the XRD analysis as discussed above. At very high current density (1600 mAh/g), the plateau related to the reduction of Fe^{3+} and Fe^{2+} to Fe^0 (≈0.8 V) is less defined compared to that at lower current density, which is due to polarization (Figure 10c).

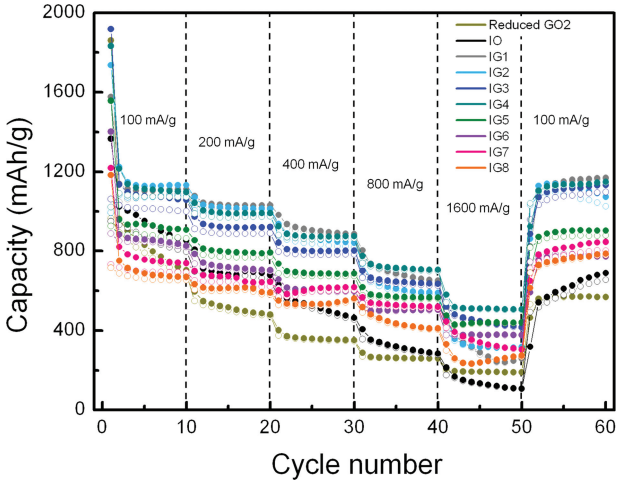

Figure 9. Rate properties of reduced GO2, IO and IG1-IG8 produced by the benzyl alcohol route.

Figure 10d shows the rate properties of IG1, IG2, and IG3. The cristallite sizes are similar for all composites (~6.0 nm; see Table 1). The first discharge of reduced GO2 by the "benzyl alcohol route" delivers 1861 mAh/g while its first charge delivers 964 mAh/g, with an initial Coulombic efficiency of 51.8%. The initial Coulombic efficiency of IG1, IG2 and IG3 are 63.0, 57.3, and 55.3%, respectively. This points out that a higher reduced graphene oxide content lowers the initial Coulombic efficiency. Moreover, the amount of reduced graphene oxide content has a certain impact on the rate properties too. The reversible capacities of IG1 are comparable to that of IG2 and higher than that of IG3 at low current density (100 mA/g). For higher current densities, however, the IG1 sample drastically lowers its performance compared to the IG3 sample. This is attributed to the increase of the conductivity of the electrode with the amount of reduced graphene oxide, due to the improvement of the electrical contact between the current collector and the active material (i.e., iron oxide nanoparticles/reduced graphene oxide). Figure 10e shows the second charge and discharge profiles of reduced GO2 by benzyl alcohol, IG1, IG2, and IG3 at a current density of 100 mA/g. The shape of the charge and discharge profiles of reduced graphene oxide is consistent with that reported in literature.[11,13,14,51] The largest portion of the discharge capacity is delivered under 0.5 V similarly to regular graphite but without the appearance of the typical staged reduction plateaus. It is clearly observed that the capacity delivered at plateau decreases and the capacity under 0.8 V increases as the graphene content increases in voltage profiles of the composites (i.e., IG1-IG3). Similarly, the capacity under 0.8 V increases as the reduced graphene oxide content increases, even at very

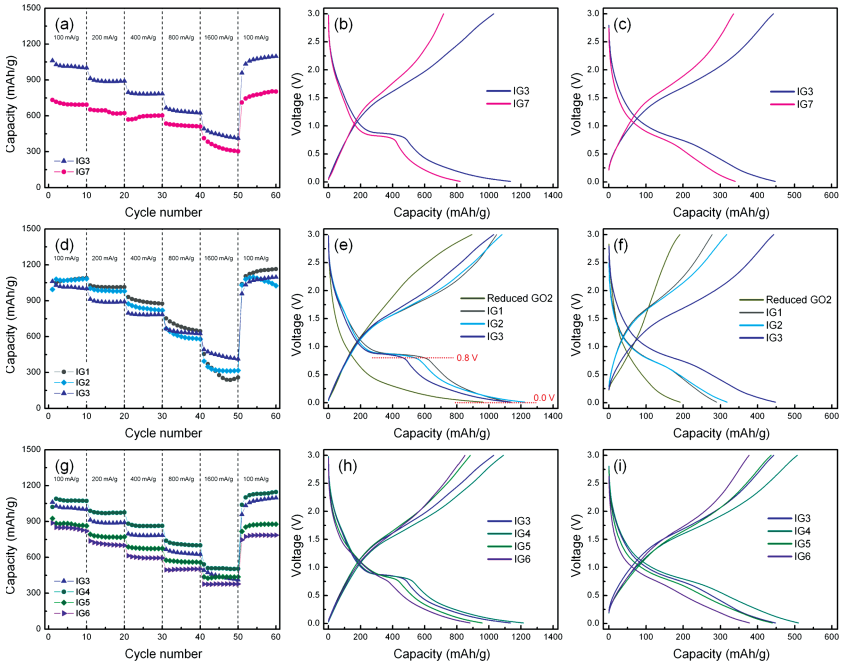

Figure 10. Rate properties of: a) IG3 and IG7, d) IG1-IG3 and g) IG3-IG6. Only charge (delithiation) capacities are reported. The charge/discharge profiles at current density of 100 mA/g (2nd cycle) are plotted in (b), (e) and (h) while the charge/discharge profiles at current density of 1600 mA/g (45th cycle) are plotted in (c), (f) and (i). Red dotted lines are used as a guide to the eye in panel (e).

high current density (Figure 10f). However, the capacity delivered at plateau of IG3 is the highest and those of IG1 and IG2 are similar. This indicates that the contribution of iron oxide to the overall capacity is higher for higher reduced graphene oxide contents, especially at high current density.

After having optimized the reduced graphene oxide content in the composites, the iron oxide average particle size is varied in order to obtain the highest performance in terms of capacity and specific current densities. Figure 10g presents the rate properties of IG3-IG6 (different synthesis temperatures, so different iron oxide average particle size, cf. Table 1). All the samples are very stable even at high current density and all have very high specific capacities (800–1200 mAh/g at a current density of 100 mA/g). The initial Coulombic efficiencies of IG3, IG4, IG5 and IG6 are 55.3, 55.7, 59.5, and 63.3%, respectively. This behavior can be ascribed to the reduced graphene oxide effect on the Coulombic efficiency as already discussed above. The sample IG4 shows the best overall performances in terms of specific capacity, rate capability and cycle stability. The capacity drops with the increase of the current density from 100 to 1600 mA/g of IG3, IG4, IG5 and IG6 are 56.3, 52.9, 50.6, and 55.5%, respectively. The capacity drop has been calculated according to the following equation:

$$C_{drop}(\%) = C_{ch\,arge}^{5th} - C_{ch\,arge}^{45th} \Big/ C_{ch\,arge}^{5th} * 100 \quad (1)$$

The second charge and discharge profiles of IG3-IG6 are shown in Figure 10h. Well-defined plateaus are visible in the discharge profiles of IG3 and IG4. The broadened and ambiguous plateaus in the discharge profiles of IG5 and IG6 can be related to the crystallite/particle sizes of iron oxide (*cf.* Table 1). Especially, the plateau is almost not observed in the discharge profile of IG6. The low specific capacity at low current density seems to be related to the amount of impurities such as oxygen-containing functional groups from the weight loss from 200 to 300 °C in TGA experiments. The oxygen-containing functional groups of reduced graphene oxide may contribute less to the reversible capacity as it has been reported in a recent paper.[13] The trend of voltage profiles at very high current density (Figure 10i) is similar to that at low current density. The electron conductivity is already optimized by high reduced graphene oxide content and, because the iron oxide particles are well dispersed onto the reduced graphene oxide, the iron oxide particle size does not greatly affect the electrochemical properties.

In order to further understand the electrochemical properties of iron oxide/reduced graphene oxide nanocomposites, electrochemical impedance spectroscopy measurements (EIS) were performed at the charged state after 10 cycles (**Figure 11**). The EIS spectra were fitted with the equivalent circuit shown in the inset of Figure 11. The semicircles visible in the high and middle frequency ranges indicate the SEI (R_{SEI}) and charge transfer (R_{ct}) resistances respectively. The EIS spectra clearly show that IG1, IG2, IG5, and IG6 reach the highest values of SEI resistances. These results are addressed to the higher surface areas of these samples since larger areas promote the formation of the organic layer with a large first cycle irreversible loss (Figure 9). However, the formation of such a layer does not seem to affect the electrode performances, for example IG1 is one of the best performing composites among our materials.

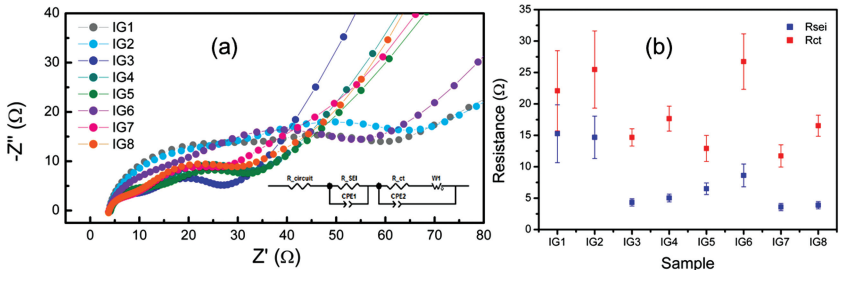

Figure 11. a) Nyquist plots of IG1-IG8 composites after cycling. b) SEI and charge transfer resistances calculated from impedance fitting. The equivalent circuit used for the fitting is shown in the inset of (a).

2.4. General Discussion

On the basis of TEM observations only (Figure 5h), one could assume that IG5

would be a high performing electrode material prepared under the mildest synthesis conditions, and having the smallest particle sizes and a very good particle distribution over the carbonaceous support. However, IG5 performs quite poorly, in terms of specific capacity, with respect to the legitimate expectations its morphology could allow (see Figure 9 and 10 and corresponding discussion). This could possibly be ascribed to a full coverage of the RGO with crystallites as also suggested by the high SEI resistance estimated from impedance spectroscopy results seem to point out (Figure 11). Moreover, IG5 shows the smallest charge transfer resistance which is typically linked to the electron exchange process at the surface of the electrode material with ions coming from the electrolyte. If one correlates this observation with the BET surfaces areas (IG5 also possesses the highest surface area for the IG3 to IG5 series, see Table 1) the presence of these small particles becomes quite clear. This leads to conclude that for optimal electrochemical performances (i.e., a satisfactory compromise between capacity and rate capability) a better crystallinity (i.e., a slightly larger average particle size) is preferred, which is found when the microwave assisted synthesis is performed in the temperature range between 200 and 220 °C.

As already pointed out, the IG4 composite showed the best performance compromise between the samples discussed in this article. This sample was prepared with GO2 at the highest temperature (220 °C), it has an average crystallite size of 5.6 nm, it has one of the lowest surface areas and the lowest I_D/I_G ratio (close to 1.2). The higher reaction temperature increases the crystallinity of the particles which is crucial for maximizing the ionic exchange during the electrochemical reactions. The lower overall surface area hinders the formation of the SEI layer limiting the electrolyte consumption over prolonged cycling. The charge transfer resistance for IG4 is together with the one of IG3, 5, 7 and 8 around 15 Ω. Samples with lower GO content (IG1 and IG2) suffer some hindrance in the electron transfer from the carbonaceous substrate to the surface of the particles while samples with very low crystallinity (i.e., IG6) clearly present both a high SEI and charge transfer resistances.

In general, our composite materials display very high specific capacities and excellent rate capabilities even compared to other previous reported iron oxide/reduced graphene oxide composites electrodes (**Table 3**). It is remarkable that IG3 and, even better, IG4, have not only high reversible capacity at both low and high current densities but also outstanding cycle stability, which is difficult to obtain in high specific capacity anodes. Table 3 compares the reversible capacities recently published by various groups for iron oxide/reduced graphene oxide composites. Although a direct comparison is not trivial due to different measurements parameters and anode preparations, it is also clear that our optimized sample (IG4), fabricated following a meticulous study of the structure-properties relationship, is among the best reported so far. The iron oxide/reduced graphene oxide composite performing the closest to IG4 is that reported by Su et al.[60] The electrochemical results, although not perfectly comparable, suggest a better cycling performance of the IG4 composite which displays no capacity fading after 60 cycles.

Table 3. Reversible capacities of iron oxide/reduced graphene oxide composites as anode materials.

Iron oxide type	Reversible capacity at low current density	Reversible capacity at high current density	Reference
α-Fe_2O_3	~1000 mAh/g at 0.l C	~550 mAh/g at 2 C	[52]
α-Fe_2O_3	~800 mAh/g at 100 mA/g	-	[53]
α-Fe_2O_3	~1150 mAh/g at 100 mA/g	~750 mAh/g at 800 mA/g	[54]
α-Fe_2O_3	~800 mAh/g at 0.1 C	~600 mAh/g at 1 C	[55]
Fe_3O_4	~1000 mAh/g at 35 mA/g	~500 mAh/g at 1750 mA/g	[7]
Fe_3O_4	~700 mAh/g at 100 mA/g	-	[56]
Fe_3O_4	~1100 mAh/g at 100 mA/g	~400 mAh/g at 1000 mA/g	[57]
Fe_3O_4	~900 mAh/g at 100 mA/g	~600 mAh/g at 800 mA/g	[58]
Fe_3O_4	~1300 mAh/g at 0.1 C	~850 mAh/g at 4 C	[59]
Fe_3O_4	~1100 mAh/g at 100 mA/g	~500 mAh/g at 1600 mA/g	[60]
Fe_3O_4	~900 mAh/g at 0.1 C	~400 mAh/g at 2 C	[61]
Fe_3O_4	~600 mAh/g at 92.5 mA/g	-	[62]
Fe_3O_4	~1100 mAh/g at 200 mA/g	~350 mAh/g at 1600 mA/g	[63]
Fe_3O_4	~1000 mAh/g at 50 mA/g	~200 mAh/g at 2000 mA/g	[64]
Fe_3O_4	~900 mAh/g at 0.1 C	-	[65]
Fe_3O_4	~900 mAh/g at 0.2 C	~400 mAh/g at 2 C	[[66]]
Fe_3O_4	~750 mAh/g at 0.1 C	~600 mAh/g at 2 C	[67]
Fe_3O_4	~750 mAh/g at 0.2 C	~400 mAh/g at 2 C	[68]
Fe_3O_4	~800 mAh/g at 30 mA/g	~200 mAh/g at 2000 mA/g	[69]
IG4	~1050 mAh/g at 100 mA/g	~500 mAh/g at 1600 mA/g	present work

3. Conclusions

We have prepared iron oxide/reduced graphene oxide nanostructures by a simple microwave-assisted nonaqueous approach in just 5–10 min. This straightforward synthesis method, allowed us to study many samples, having different characteristics in terms of reduced graphene oxide support type, compositional ratio of reduced graphene oxide to iron oxide, iron oxide particle size and particle density on the surface of the reduced graphene oxide. The properties of the starting graphene oxide (oxidation degree-the number of stacking layers) and reduced graphene oxide—obtained by the in situ reduction step during iron oxide deposition—are among the most important factors influencing the final electrochemical properties. The higher the compositional ratio of reduced graphene oxide to iron oxide is, the higher the rate performance. The particle size has less influence on the electrochemical properties. Finally, by this process of assessing the structure-properties relationship based on a large number of samples, we could obtain iron oxide/reduced graphene oxide composites having the best compromise in terms of specific capacity, rate capability and cycle stability reported so far.

4. Experimental Section

Chemicals: Iron(III) acetylacetonate, $Fe(acac)_3$, (≥99.9% trace metals basis), benzyl alcohol (≥99%, reagentplus), graphite (powder, <20 μm,

synthetic), phosphorus pentoxide (99%, reagentplus) were purchased from Sigma-Aldrich. $NaNO_3$, H_2SO_4, $KMnO_4$, H_2O_2 and HCl were purchased from Samchun Chemical. All the chemicals were used as received.

Preparation of Graphene Oxide by the Hummers' Method: Graphene oxide (GO) was synthesized from graphite powder (<20 μm) following the Hummers' method.[70] Specifically, 1 g of graphite was put into a solution of concentrated H_2SO_4 (46 mL) and 1 g of $NaNO_3$ and it was stirred in an ice bath for 2 h. 6 g of $KMnO_4$ were slowly added and reacted for 2 h. After the mixture was stirred vigorously for 24 h at room temperature, 250 mL of DI water was added. The solution was then heated to 98 °C and maintained at this temperature for 1 h. Then, 6 mL of H_2O_2 (30 wt%) were slowly added and the solution was filtered and washed with 1:10 HCl aqueous solution to remove metal ions, followed by repeated washings with water. The solid phase was then separated by centrifugation. Finally, the precipitate was dried at 60 °C overnight. GO prepared by the Hummer's method is denoted as GO1 in this work.

Preparation of Graphene Oxide by the Modified Hummers' Method: GO was also prepared by a modified Hummers' method.[71] First, 3 g of graphite, 5 g of $K_2S_2O_8$ and 5 g of P_2O_5 were stirred together in 40 mL concentrated H_2SO_4 for 5 h at 80 °C. After it was cooled naturally, the mixture was filtered with DI water, and dried at 70 °C overnight. The pre-oxidized graphite powder (3 g) was put into 120 mL H_2SO_4 kept a low temperature in a water ice bath. After 15 g $KMnO_4$ was slowly added to the mixture, it was just stirred for 4 h and 250 mL DI water was added. Finally, 10 mL H_2O_2 (30 wt%) was added and then the color of the mixture changed to yellow. The mixture was filtered and washed with 1:10 HCl aqueous solution and then water to remove the acid. The obtained brown colored powder was dried at 60 °C overnight. GO prepared by the modified Hummers' method is denoted as GO2 in this work.

Non-Aqueous Sol-Gel Synthesis of Iron Oxide and Iron Oxide/Reduced Graphene Oxide Composites: For the synthesis of iron oxide, $Fe(acac)_3$ was added to 20 mL of benzyl alcohol in a vial of a total capacity of 35 mL and sealed with a Teflon cap under inert argon atmosphere. For the synthesis of iron oxide/graphene composites, graphene oxide was also added to the same reaction mixture. The solutions were homogenized by vigorous stirring for 30 seconds and sonication for 2 h. The solutions were exposed to microwave irradiation in a CEM Discovery SP for 5 to 10 min at 180–220 °C (Table 1). The resulting black suspensions were centrifuged and the precipitate re-dispersed and washed with ethanol (once) and dichlromethane (twice). The resulting powders were dried at 60 °C overnight.

Characterization: Transmission electron microscopy (TEM) and high-resolution TEM (HRTEM) images were obtained on a JEOL JEM-2010 and on a Tecnai F20 microscope at an accelerating voltage of 200 kV. X-ray photoelectron spectroscopy (XPS) experiments were performed in an UHV multipurpose surface analysis system (SIGMA PROBE, ThermoFisher Scientific, UK) operating at base pressures $<10^{-10}$ mbar. For thermo-gravimetric analysis (TGA), simultaneous DTA/TGA analyser Q600 model (TA Instruments) was used with a heating rate 10 °C/min in air. The Brunauer–Emmett–Teller (BET) surface area was determined using a Micromeritics ASAP 2000 nitrogen adsorption apparatus. All the samples were degassed at 200 °C prior to BET measurements. Powder X-ray diffractometry (XRD) was performed in the Bragg-Brentano geometry using a PANalytical X'Pert Powder diffractometer equipped with Cu radiation (154.18 pm) and set to 45 kV/40 mA. The machine was calibrated with LaB_6 standard powder. A second Ni filter was placed on the incident beam in order to help reducing fluorescence effects. Powders were loaded in a diffraction-free silicon sample holder. Data for the Rietveld refinement were collected in a step scan mode in the range $10 < 2\theta < 100°$ with a step of 0.08° 2θ. The counting time was fixed to 60 s/step for all samples.

Rietveld Refinement Procedure: The program FullProf was used for crystal structure refinements, employing the Rietveld method.[72] The collected XRD data of the various iron oxide composites were refined in the space group $Fd\,\bar{3}m$ starting from the model given by the JCPDS database.

In the particular case of our composites, reduced graphene oxide, which is lacking of a well-defined crystal structure, was replaced in the treatment by graphite according to the JCPDS file #04-014-0362 (hexagonal lattice $P6_3/mmc$ with a = 246.47 pm and c = 675.30 pm). The refinements were performed with the TCH pseudo-Voigt profile function and instrumental broadening was taken into account by fitting a standard LaB_6 sample with the same kind of profile function (U = 0.014(1); V = –0.021(1); W = 0.011(1); X = 0.067(2)). The full width at half-maximum (FWHM) parameters of the Gaussian (H_G) and Lorentzian (H_L) components of the peak profile that we have used have an angular dependence given by:

$$H_G^2 = \left[U + (1-\xi)^2 D_{ST}^2(a_D)\right]\tan^2\theta + V\tan\theta + W \quad (2)$$

$$H_L = \left[X + \xi D_{ST}(a_D)\right]\tan\theta + \frac{Y}{\cos\theta} \quad (3)$$

Where the parameters in the above formulae have a meaning in terms of strains (U, α_D, X) or size (Y) of the crystallites. The function D_{ST} (α_D) has been given by Stephens,[73] while the parameter ξ is a mixing coefficient to simulate the Lorentzian contributions to strains. The standard deviations reported for the average crystallite sizes (Table 1) are a measure of the degree of anisotropy and not of the estimated error. Moreover, cubic harmonic functions were applied to every iron oxide composite.

In order to calculate the distribution functions for the nanometric particles in our samples, X-ray line broadening were analysed by the Breadth computer program.[74] The Breadth program calculates microstructural parameters according to the Warren–Averbach and simplified integral breadth methods. The X-ray line broadening of the most intense iron oxide reflections (namely 220, 311, 400, 422, 511, and 440) was analyzed. Input data for the Breadth program, such as peak positions ($2\theta°$), FWHM and Lorenz–Gauss mixing coefficient (η), were taken from the output of the FullProf program. This same procedure has already proved to be effective for other materials.[75,76] Briefly, particle size distribution functions obey to log-normal equations in the form:

$$f(x) = \frac{1}{\sqrt{2\pi}\ln\sigma}\frac{1}{x}\exp\left\{-\frac{\left[\ln\left(\frac{x}{m}\right)\right]^2}{2\ln\sigma^2}\right\} \quad (4)$$

where x is the particle size, σ is the variance and m is the median of the $f(x)$ function. For detailed description of the calculations, we refer to refs [76,77].

Electrochemical Characterization: Working electrodes were prepared from a n-methyl-2-pyrrolidinone slurry of the defined sample (see Table 1), Super P carbon conducting agent and polyvinylidene fluoride binder in the 70:15:15 weight ratio. The slurry was cast onto a copper foil using a doctor blade and then pressed for electrochemical testing. 2016 coin-type half-cells were assembled in an argon-filled glove box using lithium foil as both counter and reference electrodes. 1.0 M $LiPF_6$ in ethylene carbonate and diethyl carbonate (1:1 volume ratio) was used as electrolyte. The cells were galvanostatically discharged and charged at room temperature in the 3.0 to 0.01 V vs Li^+/Li voltage range using a WBCS3000 (WonA Tech, Korea) apparatus. Electrochemical impedance spectroscopy measurements were carried out in the range of the frequency from 100 kHz to 50 mHz with an AC signal amplitude of 5 mV.

Supporting Information

Supporting Information is available from the Wiley Online Library or from the author.

Acknowledgements

This work was partially supported by the WCU (World Class University) program through the National Research Foundation (NRF) of Korea funded by the Ministry of Education, Science and Technology (R31-10013) and FCT project PTDC/CTM-NAN/110776/2009. Y.-E. Sung acknowledges financial support by Korea Ministry of Education, Science,

and Technology through the Institute of Basic Science (IBS) program. Dr. Patrícia Russo from the University of Aveiro is acknowledged for critical reading of the manuscript and fruitful discussion.

Received: January 1, 2013
Published online: April 5, 2013

[1] M. Winter, R. J. Brodd, *Chem. Rev.* **2004**, *104*, 4245–4269.
[2] K. Kang, Y. S. Meng, J. Breger, C. P. Grey, G. Ceder, *Science* **2006**, *311*, 977–980.
[3] M. Armand, J.-M. Tarascon, *Nature* **2008**, *451*, 652–657.
[4] D. Wang, D. Choi, J. Li, Z. Yang, Z. Nie, R. Kou, D. Hu, C. Wang, L. V. Saraf, J. Zhang, I. A. Aksay, J. Liu, *ACS Nano* **2009**, *3*, 907–914.
[5] H. Wang, L.-F. Cui, Y. Yang, H. S. Casalongue, J. T. Robinson, Y. Liang, Y. Cui, H. Dai, *J. Am. Chem. Soc.* **2010**, *132*, 13978–13980.
[6] Z.-S. Wu, W. Ren, L. Wen, L. Gao, J. Zhao, Z. Chen, G. Zhou, F. Li, H.-M. Cheng, *ACS Nano* **2010**, *4*, 3187–3194.
[7] G. Zhou, D.-W. Wang, F. Li, L. Zhang, N. Li, Z.-S. Wu, L. Wen, G. Q. Lu, H.-M. Cheng, *Chem. Mater.* **2010**, *22*, 5306–5313.
[8] S.-K. Park, S.-H. Yu, N. Pinna, S. Woo, B. Jang, Y. -H. Chung, Y.-H. Cho, Y. -E. Sung, Y. Piao, *J. Mater. Chem.* **2012**, *22*, 2520–2525.
[9] M. Liang, L. Zhi, *J. Mater. Chem.* **2009**, *19*, 5871–5878.
[10] J. K. Lee, K. B. Smith, C. M. Hayner, H. H. Kung, *Chem. Commun.* **2010**, *46*, 2025–2027.
[11] E. Yoo, J. Kim, E. Hosono, H.-s. Zhou, T. Kudo, I. Honma, *Nano Lett.* **2008**, *8*, 2277–2282.
[12] G. Wang, X. Shen, J. Yao, J. Park, *Carbon* **2009**, *47*, 2049–2053.
[13] D. Pan, S. Wang, B. Zhao, M. Wu, H. Zhang, Y. Wang, Z. Jiao, *Chem. Mater.* **2009**, *21*, 3136–3142.
[14] X. Tong, H. Wang, G. Wang, L. Wan, Z. Ren, J. Bai, J. Bai, *J. Solid State Chem.* **2011**, *184*, 982–989.
[15] H. Kim, M. Seo, M.-H. Park, J. Cho, *Angew. Chem. Int. Ed.* **2010**, *49*, 2146–2149.
[16] C. Kim, M. Noh, M. Choi, J. Cho, B. Park, *Chem. Mater.* **2005**, *17*, 3297–3301.
[17] S. Baek, S.-H. Yu, S.-K. Park, A. Pucci, C. Marichy, D.-C. Lee, Y. -E. Sung, Y. Piao, N. Pinna, *RSC Adv.* **2011**, *1*, 1687–1690.
[18] N. Pinna, S. Grancharov, P. Beato, P. Bonville, M. Antonietti, M. Niederberger, *Chem. Mater.* **2005**, *17*, 3044–3049.
[19] J. Ba, J. Polleux, M. Antonietti, M. Niederberger, *Adv. Mater.* **2005**, *17*, 2509–2512.
[20] M. Niederberger, G. Garnweitner, *Chem.–Eur. J.* **2006**, *12*, 7283–7302.
[21] N. Pinna, M. Niederberger, *Angew. Chem. Int. Ed.* **2008**, *47*, 5292–5304.
[22] N. Pinna, *J. Mater. Chem.* **2007**, *17*, 2769–2774.
[23] N. Pinna, M. Karmaoui, M. -G. Willinger, *J. Sol-Gel Sci. Technol.* **2011**, *57*, 323–329.
[24] I. Bilecka, I.; M. Djerdj, M. Niederberger, *Chem. Commun.* **2008**, 886–888.
[25] I. Bilecka, P. Elser, M. Niederberger, *ACS Nano* **2009**, *3*, 467–477.
[26] H.-K. Jeong, Y. P. Lee, W. E. Lahaye, M.-H. Park, K. H. An, I. J. Kim, C.–W. Yang, C. Y. Park, R. S. Ruoff, Y. H. Lee, *J. Am. Chem. Soc.* **2008**, *130*, 1362–1366.
[27] C. Pecharroman, T. Gonzalez-Carreno, J. E. Iglesias, *Phys. Chem. Miner.* **1995**, *22*, 21–29.
[28] R. M. Cornell, U. Schwertmann, *The Iron Oxides: Structure, Properties, Reactions, Occurrences, And Uses*, Wiley–VCH, Weinheim **2003**, p. 32.
[29] M. Pernet, P. Strobel, B. Bonnet, P. Bordet, *Solid State Ionics* **1993**, *66*, 259–265.
[30] N. Pinna, G. Garnweitner, M. Antonietti, M. Niederberger, *J. Am. Chem. Soc.* **2005**, *127*, 5608–5612.
[31] H. M. Ho, E. Goo, G. J. Thomas, *Appl. Phys.* **1986**, *59*, 1606–1610.
[32] A. K. Kercher, D. C. Nagle, *Carbon* **2003**, *41*, 15–27.
[33] M. Wilke, G. M. Partzsch, R. Bernhardt, D. Lattard, *Chem. Geol.* **2005**, *220*, 143–161.
[34] S. Trudel, E. D. Crozier, R. A. Gordon, P. S. Budnik, R. H. Hill, *J. Solid State Chem* **2011**, *184*, 1025–1035.
[35] S. H. Choi, B. R. Wood, A. T. Bell, M. T. Janicke, K. C. Ott, *J. Phys. Chem. B* **2004**, *108*, 8970–8975.
[36] T. Yamamoto, *X-Ray Spectrom.* **2008**, *37*, 572–584.
[37] I. Arcon, J. Kolar, A. Kodre, D. Hanzel, M. Strlic, *X-ray Spectrom.* **2007**, *37*, 199–205.
[38] T. Yamashita, P. Hayes, *Appl. Sur. Sci.* **2008**, *254*, 2441–2449.
[39] C. Marichy, J.-P. Tessonnier, M. C. Ferro, K.-H. Lee, R. Schlogl, N. Pinna, M.-G. Willinger, *J. Mater. Chem.* **2012**, *22*, 7323–7330.
[40] S. Hariharan, K. Saravanan, P. Balaya, *Electrochem.Solid-State Lett.* **2010**, *13*, A132–A134.
[41] P. L. Taberna, S. Mitra, P. Poizot, P. Simon, J.-M. Tarascon, *Nat. Mater.* **2006**, *5*, 567–573.
[42] W.-M. Zhang, X.-L. Wu, J. -S. Hu, Y. -G. Guo, L.-J. Wan, *Adv. Funct. Mater.* **2008**, *18*, 3941–3946.
[43] Y. Piao, H. S. Kim, Y.-E. Sung, T. Hyeon, *Chem. Commun.* **2010**, *46*, 118–120.
[44] T. Yoon, C. Chae, Y.-K. Sun, X. Zhao, H. H. Kung, J. K. Lee, *J. Mater. Chem.* **2011**, *21*, 17325–17330.
[45] S. Jin, H. Deng, D. Long, X. Liu, L. Zhan, X. Liang, W. Qiao, L. Ling, *J. Power Sources* **2008**, *183*, 717–723.
[46] Z. Yang, J. Shen, N. Jayaprakash, L. A. Archer, *Energy Environ. Sci.* **2012**, *5*, 7025–7032.
[47] Z. Wang, D. Luan, S. Madhavi, C. M. Li, X. W. Lou, *Chem. Chemmun.* **2011**, *47*, 8061–8063.
[48] M. M. Thackeray, W. I. F. David, J. B. Goodenough, *Mater. Res. Bull.* **1982**, *17*, 785–793.
[49] J. Cabana, L. Monconduit, D. Larcher, M. R. Palacin, *Adv. Mater.* **2010**, *22*, E170–E192.
[50] G. Wang, B. Wang, X. Wang, J. Park, S. Dou, H. Ahn, K. J. Kim, *Mater. Chem.* **2009**, *19*, 8378–8384.
[51] P. Lian, X. Zhu, S. Liang, Z. Li, W. Yang, H. Wang, *Electrochim. Acta* **2010**, *55*, 3909–3914.
[52] M. Zhang, B. Qu, Y. Chen, X. Yu, L. Chen, Q. Li, Y. Wang, T. J. Wang, *Mater. Chem.* **2012**, *22*, 3868–3874.
[53] D. Chen, W. Wei, R. Wang, J. Zhu, L. Guo, *New J. Chem.* **2012**, *36*, 1589–1595.
[54] X. Zhu, Y. Zhu, S. Murali, M. D. Stoller, R. S. Ruoff, *ACS Nano* **2011**, *5*, 3333–3338.
[55] X.-Y. Xue, C.-H. Ma, C.-X. Cui, L.-L. Xing, *Solid State Sci.* **2011**, *13*, 1526–1530.
[56] J.-Z. Wang, C. Zhong, D. Wexler, N. H. Idris, Z.-X. Wang, L.-Q. Chen, H.-K. Liu, *Chem. Eur. J.* **2011**, *17*, 661–667.
[57] P. Lian, X. Zhu, H. Xiang, Z. Li, W. Yang, H. Wang, *Electrochim. Acta* **2010**, *56*, 834–840.
[58] D. Chen, G. Ji, Y. Ma, J. Y. Lee, J. Lu, *ACS Appl. Mater. Interfaces* **2011**, *3*, 3078–3083.
[59] S. K. Behera, *Chem. Commun.* **2011**, *47*, 10371–10373.
[60] J. Su, M. Cao, L. Ren, C. Hu, *J. Phys. Chem. C* **2011**, *115*, 14469–14477.
[61] L. Ji, Z. Tan, T. R. Kuykendall, S. Aloni, S. Xun, E. Lin, V. Battaglia, Y. Zhang, *Phys. Chem. Chem. Phys.* **2011**, *13*, 7170–7177.
[62] X. Li, X. Huang, D. Liu, X. Wang, S. Song, L. Zhou, H. Zhang, *J. Phys. Chem. C* **2011**, *115*, 21567–21573.
[63] G. Wang, T. Liu, X. Xie, Z. Ren, J. Bai, H. Wang, *Mater. Chem. Phys.* **2011**, *128*, 336–340.
[64] Y. Chen, B. Song, X. Tang, L. Lu, J. Xue, *J. Mater. Chem.* **2012**, *22*, 17656–17662.

[65] M. Zhang, D. Lei, X. Yin, L. Chen, Q. Li, Y. Wang, T. Wang, *J. Mater. Chem.* **2010**, *20*, 5538–5543.
[66] B. Li, H. Cao, J. Shao, M. Qu, *Chem. Commun.* **2011**, *47*, 10374–10376.
[67] C.-T. Hsieh, J.-Y. Lin, C.-Y. Mo, *Electrochim. Acta* **2011**, *58*, 119–124.
[68] B. Li, H. Cao, J. Shao, M. Qu, J. H. Warner, *J. Mater. Chem.* **2011**, *21*, 5069–5075.
[69] L. Tian, Q. Zhuang, J. Li, C. Wu, Y. Shi, S. Sun, *Electrochim. Acta* **2012**, *65*, 153–158.
[70] W. S. Hummers, R. E. Offeman, *J. Am. Chem. Soc.* **1985**, *80*, 1339–1339.
[71] N. I. Kovtyukhova, P. J. Ollivier, B. R. Martin, T. E. Mallouk, S. A. Chizhik, E. V. Buzaneva, A. D. Gorchinskiy, *Chem. Mater.* **1999**, *11*, 771–778.
[72] J. Rodriguez-Carvajal, *Physica B* **1993**, *192*, 55–69.
[73] P. W. Stephens, *J. Appl. Crystallogr.* **1999**, *32*, 281–289.
[74] D. Balzar, *J. Appl. Crystallogr.* **1992**, *25*, 559–570.
[75] A. Kremenovic, B. Antic, V. Spasojevic, M. Vucinic-Vasic, Z. Jaglicic, J. Pirnat, Z. Trontelj, *J. Phys. Condens. Matter* **2005**, *17*, 4285–4299.
[76] J. Gubicza, J. Szepvolgyi, I. Mohai, L. Zsoldos, T. Ungar, *Mater. Sci. Eng.* **2000**, *A280*, 263–269.
[77] T. Ungar, J. Gubicza, G. Ribarik, A. Borbely, *J. Appl. Cryst.* **2001**, *34*, 298–310.